Imaging Nucleophilic Substitution Dynamics

J. Mikosch, *et al.*

Science **319**, 183 (2008);
DOI: 10.1126/science.1150238

Science (print ISSN 0036-8075; online ISSN 1095-9203) is published weekly, except the last week in December, by the American Association for the Advancement of Science, 1200 New York Avenue NW, Washington, DC 20005.

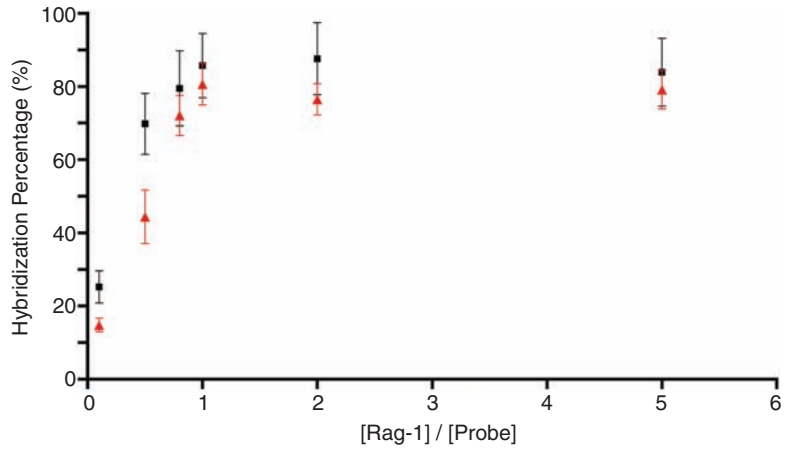

Fig. 4. Hybridization percentage as a function of the [target]/[probe] ratio. The tile used is the one shown in Fig. 3A carrying the *Rag-1* probes. Two different tile concentrations are used: 10 nM (black squares) and 200 pM (red triangles). Each error bar represents SD calculated from measurements on 50 tiles.

it should be possible to probe the spatial dependence of binding interactions involving multiple biomolecular components.

References and Notes

1. D. R. Meldrum, *Science* **292**, 515 (2001).
2. U. R. Mueller, D. V. Nicolau, *Microarray Technology and its Applications* (Springer-Verlag, Berlin, 2004).
3. M. Schena, D. Shalon, R. W. Davis, P. O. Brown, *Science* **270**, 467 (1995).
4. S. A. Bustin, T. Nolan, in *Real-Time PCR: An Essential Guide*, K. Edwards, J. Logan, N. Saunders, Eds. (Horizon Bioscience, Norfolk, UK, 2004).
5. Y. H. Yang, T. Speed, *Nat. Rev. Genet.* **3**, 579 (2002).
6. P. W. K. Rothemund, *Nature* **440**, 297 (2006).
7. Y. Chang, M. L. Brown, *Proc. Natl. Acad. Sci. U.S.A.* **96**, 191 (1999).
8. E. A. Jacobsen, O. Ananieva, M. L. Brown, Y. Chang, *J. Immunol.* **176**, 6831 (2006).
9. See supporting material on *Science* Online.
10. A. W. Peterson, R. J. Heaton, R. M. Georgiadis, *Nucleic Acids Res.* **29**, 5163 (2001).
11. Y. Gao, L. K. Wolf, R. M. Georgiadis, *Nucleic Acids Res.* **34**, 3370 (2006).
12. N. C. Seeman, *Nature* **421**, 427 (2003).
13. E. Winfree, F. Liu, L. A. Wenzler, N. C. Seeman, *Nature* **394**, 539 (1998).
14. H. Yan, S. H. Park, G. Finkelstein, J. H. Reif, T. H. LaBean, *Science* **301**, 1882 (2003).
15. K. Lund, Y. Liu, S. Lindsay, H. Yan, *J. Am. Chem. Soc.* **127**, 17606 (2005).
16. S. H. Park *et al.*, *Angew. Chem. Int. Ed.* **45**, 735 (2006).
17. M. Zuker, D. H. Mathews, D. H. Turner, in *RNA Biochemistry and Biotechnology*, J. Barciszewski, B. F. C. Clark, Eds. (Kluwer Academic, Dordrecht, Netherlands, 1999), pp. 11–43.
18. R. Chhabra *et al.*, *J. Am. Chem. Soc.* **129**, 10304 (2007).

19. This research is partly supported by funding from NIH (to S.L. and H.Y.) and from NSF, Office of Naval Research, and U.S. Air Force Office of Scientific Research (to H.Y.).

Supporting Online Material

www.sciencemag.org/cgi/content/full/319/5860/180/DC1
Materials and Methods
Sequence Information
Figs. S1 to S16

4 September 2007; accepted 21 November 2007
10.1126/science.1150082

Imaging Nucleophilic Substitution Dynamics

J. Mikosch,[1] S. Trippel,[1] C. Eichhorn,[1] R. Otto,[1] U. Lourderaj,[2] J. X. Zhang,[2] W. L. Hase,[2] M. Weidemüller,[1] R. Wester[1]*

Anion-molecule nucleophilic substitution (S_N2) reactions are known for their rich reaction dynamics, caused by a complex potential energy surface with a submerged barrier and by weak coupling of the relevant rotational-vibrational quantum states. The dynamics of the S_N2 reaction of $Cl^- + CH_3I$ were uncovered in detail by using crossed molecular beam imaging. As a function of the collision energy, the transition from a complex-mediated reaction mechanism to direct backward scattering of the I^- product was observed experimentally. Chemical dynamics calculations were performed that explain the observed energy transfer and reveal an indirect roundabout reaction mechanism involving CH_3 rotation.

Bimolecular nucleophilic substitution is a fundamental reaction mechanism in chemistry (*1*). The reaction's equation, X + R-Y → X-R + Y, summarizes bond formation by the attacking nucleophile X with the moiety R and concerted bond cleavage of the substituted leaving group Y. S_N2 reactions are widely used in preparative organic synthesis (*2*). Low-energy negative-ion reactions, most likely nucleophilic substitution, are suggested to cause the large amount of DNA double strand breaks in the wake of ionizing particles (*3*).

Anion-molecule S_N2 reactions may be the most prominent type of ion-molecule reactions, studied extensively both experimentally (*4*, *5*) and computationally (*6*, *7*). Rate coefficients for these reactions depend strongly on the surrounding solvent (*4*), making experiments on isolated gas-phase systems a crucial reference point in distinguishing solvent effects from the intrinsic dynamics of the reaction. The low rate coefficients observed in the gas phase, which are much smaller than the classical Langevin capture rate expected for a barrier-less ion-molecule reaction, are qualitatively well understood to stem from two wells (Fig. 1) on the potential energy hypersurface (*8*). This characteristic potential energy landscape is attributed to the formation of ion-dipole collision complexes on both sides of the reaction barrier. The barrier itself, which represents a transition state that corresponds to inversion at the reaction center, has a substantial influence on the reaction kinetics even though it most often lies submerged with respect to the energy of the reactants.

Studies of anion-molecule S_N2 reactions have determined reaction rates as a function of temperature (*9*, *10*) and energy (*11*) and probed the dynamics of the pre- and postreaction ion-dipole complexes (*12*, *13*). An important finding from these studies is that the reaction kinetics and dynamics are often inadequately described by statistical theories (*14*–*16*, *12*, *17*), a result supported by classical (*6*, *18*) and quantum (*19*, *7*, *20*) chemical dynamics simulations. An illustrative example of nonstatistical behavior is the strong dependence of the $Cl^- + CH_3Br$ reaction rate on the relative translational energy of the reactants, despite insensitivity to their internal temperature (*14*). Such dynamics contradict the statistical assumption of rapid randomization of all the available energy in the $Cl^- \cdot CH_3Br$ prereaction complex. Nonstatistical dynamics of the ion-dipole complexes are also evident in the product energy partitioning for the $Cl^- \cdot CH_3I$ unimolecular decomposition (*13*), the mode-specific dynamics of the $Cl^- \cdot CH_3Br$ complex (*12*, *21*), and the $Cl^- + CH_3Br$ reaction rate dependence on collision energy (*11*). Therefore, a detailed analysis of the flow of energy during the course of the reaction is required (*6*).

[1]Physikalisches Institut, Universität Freiburg, Hermann-Herder-Straße 3, 79104 Freiburg, Germany. [2]Department of Chemistry and Biochemistry, Texas Tech University (TTU), Lubbock, TX 79409, USA.

*To whom correspondence should be addressed. E-mail: roland.wester@physik.uni-freiburg.de

Until recently, many details of the S_N2 dynamics of bimolecular anion-molecule reactions could only be obtained from chemical dynamics simulations. However, with recent experimental advances (*22*), insight into the reaction dynamics may be obtained from measurements of correlated angle- and energy-differential cross sections. Specifically, the probabilities for energy redistribution within the ion-dipole complexes, their dependences on initial quantum states, the branching into different product quantum states, and the role of tunneling through the central barrier pose open questions to be probed experimentally.

We report kinematically complete reactive scattering experiments of the anion-molecule S_N2 reaction $Cl^- + CH_3I \rightarrow CH_3Cl + I^-$ (Fig. 1) with use of our ion-molecule crossed beam imaging spectrometer (*22*). In this way, we extended the successful crossed beam imaging experiments of neutrals (*23*) to ionic reactions. These single-collision experiments measure directly the velocity vector of the product anion, which reveals the energy- and angle-differential reaction cross section. By using reactants with well-defined relative kinetic energy and momentum, we can determine energy transfer during the reaction, which yields the fraction of total available energy partitioned to internal modes of the molecular product. For comparison with the experimental results, we have performed high-level trajectory simulations.

In the experiment, we produced slow pulses of Cl^- anions with a tunable well-defined kinetic energy between 0.2 and 5 eV in a compact electron-impact supersonic expansion ion source (*22*). The ion pulses crossed a supersonic neutral jet of CH_3I seeded in helium, whereby a few of the Cl^- anions induced nucleophilic substitution and liberated I^- anions. The interaction region of the crossed beam experiment was placed in a pulsed-field velocity map imaging spectrometer, which maps the velocity of the I^- product anion

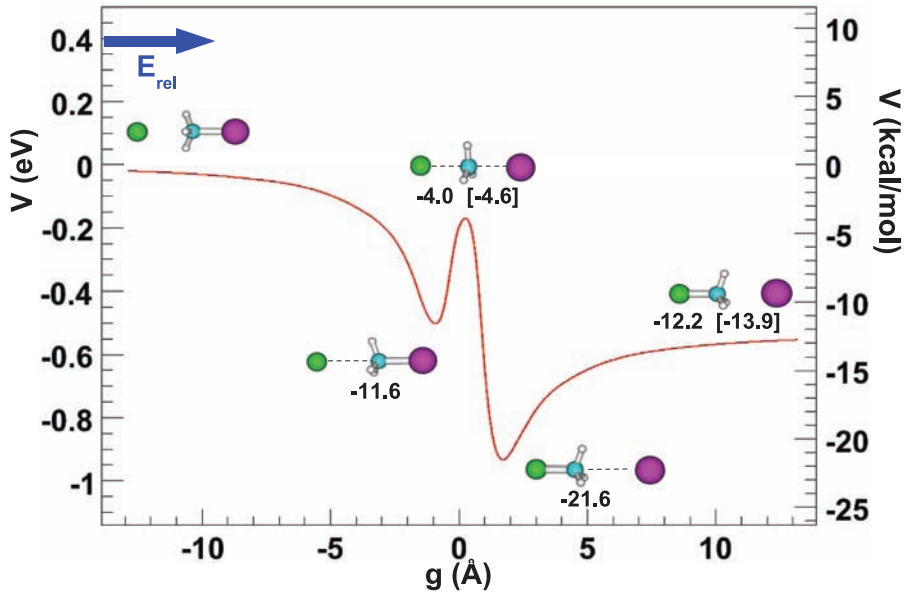

Fig. 1. Calculated MP2(fc)/ECP/aug-cc-pVDZ Born-Oppenheimer potential energy along the reaction coordinate $g = R_{C-I} - R_{C-Cl}$ for the S_N2 reaction $Cl^- + CH_3I$ and obtained stationary points. The reported energies do not include zero-point energies. Values in brackets are from (*28*).

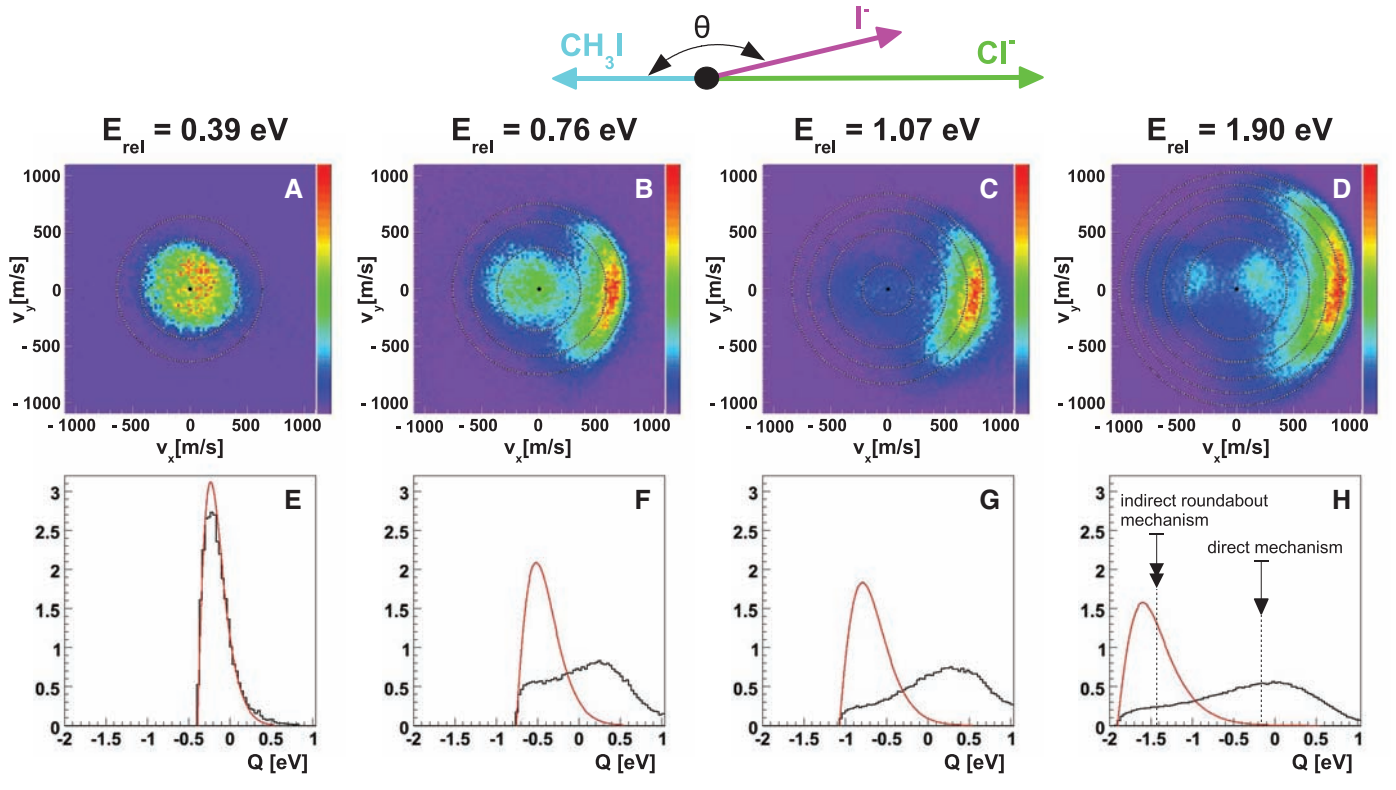

Fig. 2. (**A** to **D**) Center-of-mass images of the I^- reaction product velocity from the reaction of Cl^- with CH_3I at four different relative collision energies. The image intensity is proportional to $[(d^3\sigma)/(dv_x\, dv_y\, dv_z)]$: Isotropic scattering results in a homogeneous ion distribution on the detector. (**E** to **H**) The energy transfer distributions extracted from the images in (A) to (D) in comparison with a phase space theory calculation (red curve). The arrows in (H) indicate the average Q value obtained from the direct chemical dynamics simulations.

onto a position-sensitive detector. With the use of slice imaging (*23*) implemented by activating the detector only during a short time window, we imaged only scattering events for which the velocity vectors of the products lie within the plane defined by the reactant velocities. Because of the cylindrical symmetry of the scattering cross section, this procedure yielded the velocity magnitude- and angle-differential cross sections directly, without resorting to Abel-inversion-type algorithms. The neutral product does not need to be detected because its properties can be inferred from conservation of energy and momentum (*24*).

The top row of Fig. 2 shows maps of the I^- product ion velocities from the $Cl^- + CH_3I \rightarrow CH_3Cl + I^-$ reaction at four different relative collision energies between E_{rel} = 0.39 eV and E_{rel} = 1.90 eV, which were chosen because they span the distinct reaction dynamics observed in this energy range. The only data processing applied to the ion impact position on the detector is a linear conversion from position to ion speed and a transformation into the center of mass frame. Consequently, the velocity vectors of the two reactants, the Cl^- anion and the CH_3I neutral, line up horizontally and point in opposite directions, indicated by the arrows in Fig. 2. Each velocity image represents a histogram summed over 10^5 to 10^6 scattering events. The total energy available to the reaction products is given by the relative translational energy, E_{rel}, of the reactants plus the exoergicity, 0.55 eV, of the reaction (Fig. 1). I^- products reach the highest velocity when all the available energy is converted to translational energy. The outermost circle in Fig. 2 represents this kinematic cutoff for the velocity distribution. The other concentric rings display spheres of the same translational energy and hence also the same internal product excitation, spaced at 0.5-eV intervals.

The images in Fig. 2 reveal many details of the reaction dynamics. For the lowest relative collision energy of 0.39 eV, there is an isotropic distribution of product velocities centered around zero with all scattering angles equally probable. This pattern points to the traditional reaction mechanism (*8*) mediated by a collision complex whose lifetime is long compared to the time scale of its rotation. The complex-mediated mechanism is accompanied by a velocity distribution that drops to zero far before the kinematic cutoff is reached, as can be inferred from the position of the outermost ring in the image. Thus, the largest fraction of the available energy is partitioned to internal rovibrational energy of the CH_3Cl product.

A distinctly different reaction mechanism becomes dominant at the higher relative collision energy of 0.76 eV (Fig. 2B): The I^- product is back-scattered into a small cone of scattering angles. This pattern indicates that direct nucleophilic displacement dominates. The Cl^- reactant attacks the methyl iodide molecule at the concave center of the CH_3 umbrella and thereby drives the I^- product away on the opposite side. The direct mechanism leads to product ion velocities close to the kinematic cutoff. In addition, part of the product flux is found at small product velocities with an almost isotropic angular distribution, indicating that for some of the collisions there is a significant probability of forming a long-lived complex.

At a collision energy of 1.07 eV (Fig. 2C), the complex-mediated reaction channel is not observed any more. The reaction proceeds almost exclusively by the direct mechanism, with a similar velocity and a slightly narrower angular distribution relative to the 0.76-eV case. At an even higher collision energy of 1.90 eV, the dominating backward scattering pattern of the I^- ion spreads over an increased range of scattering angles. The inserted rings demonstrate a concomitant broadening of the velocity distribution. In addition, a new feature appears that consists of two distinct low-velocity peaks symmetric in the forward and the backward directions with respect to the center of mass. As detailed below, these peaks represent reactions that occur via a roundabout mechanism. At relative energies above 2 eV, new dissociative channels open and influence the scattering dynamics, and so we restricted the current presentation to collision energies up to 1.9 eV.

For a quantitative analysis, we calculated the energy transfer $Q = E_{kin,final} - E_{kin,initial}$ for the reaction events. For the lowest collision energy of 0.39 eV, Fig. 2E shows that the observed distribution vanishes for Q values far below the kinematic cutoff at +0.55 eV. A theoretical phase-space calculation (red line in Fig. 2E) (*25*), which assumes that the available energy is distributed statistically among all degrees of freedom of the reaction products, shows excellent agreement with the data after convolution with the experimental resolution stemming from the velocity spread of the reactant beams. The observation of statistical energy partitioning at this finite collision energy is unexpected, given the reported nonstatistical unimolecular decomposition of metastable $Cl^-{\cdot}CH_3I$ S_N2 complexes (*13*). We found that 84% of the total available energy is trapped in internal excitation of the CH_3Cl reaction product, which amounts to E_{int} = 0.79 eV. At all the higher relative collision energies (Fig. 2, F to H), the phase space model cannot reproduce the observed dynamics. Here, the Q value distribution peaks near its maximum value of +0.55 eV. The mean internal excitation in absolute and in relative numbers is given by 0.5 eV (40%), 0.45 eV (25%), and 0.95 eV (40%). At 1.07 eV relative collision energy, a minimum is found both in the absolute and the relative amount of internal excitation, which is a sign of subtle changes in the translation-vibration coupling during the reaction.

To complement the above experimental study of the $Cl^- + CH_3I$ reaction dynamics, we performed a trajectory simulation at the MP2(fc)/ECP/aug-cc-pVDZ (*26*) level of theory by a computational approach directly using this theory (*27*). As shown in Fig. 1, this theory gives energies for the reaction's stationary points in good agreement with previous values based on rate coefficient measurements (*28*). These simulations are computationally expensive and only practical at the highest collision energies where both the encounter time is short and the reaction probability appreciable. Here, we report results for the 1.9-eV collision energy and CH_3I rotational and vibrational temperatures of 75 K and 360 K, respectively, which are the approximate experimental conditions.

Although the reaction has no overall barrier, the simulations show a quite low reaction probability at 1.9 eV, decreasing from 0.065, 0.05,

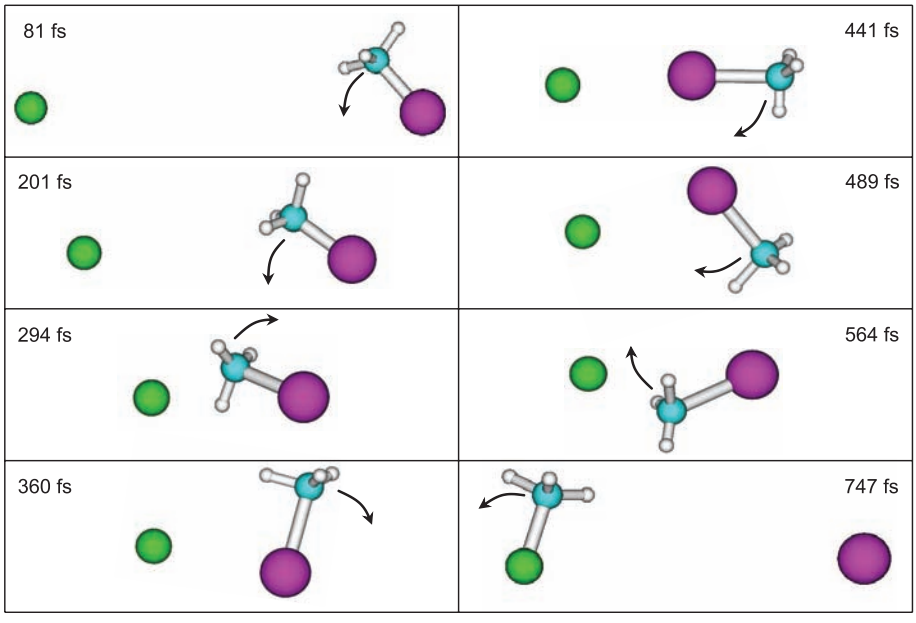

Fig. 3. View of a typical trajectory for the indirect roundabout reaction mechanism at 1.9 eV that proceeds via CH_3 rotation.

0.03, to 0.005 as the collision impact parameter, b, is increased from 0.0, 1.0, 2.0, to 3.0 Å. On the basis of the centrifugal potential at the central barrier, the maximum impact parameter for reaction is estimated as 5.2 Å, but the low reaction probability at $b > 2$ Å makes it computationally intractable to sample the complete range of b. Nevertheless, important details of the reaction dynamics are found. The reaction occurs by both direct and indirect mechanisms, with a direct fraction of 0.4, 0.8, 0.8, and ~1.0 for impact parameters of 0.0, 1.0, 2.0, and 3.0 Å, respectively, suggesting the direct reaction dominates at the larger b values. The product energy partitioning for the direct reaction is the same for these four impact parameters, with average fractions of 0.04, 0.23, and 0.73 for rotation, vibration, and translation, respectively. For the indirect trajectories, the average fractions of energy partitioning to rotation (0.28), vibration (0.56), and translation (0.16) are quite different. Because the direct reaction is expected to dominate when trajectories are averaged over all impact parameters, an overall fraction partitioned to translation in the range of 0.6 to 0.7 is expected. This partitioning corresponds to a mean internal excitation of about 0.85 eV, which agrees well with the experimental value of 0.95 eV as given above. The much higher internal excitation for indirect reactions amounts to about 1.9 eV, which is in good agreement with the average energy of the two low-velocity peaks observed in the experiment (Fig. 2D and Fig. 2H, left arrow).

The atomic-level mechanisms for the direct and indirect reactions at 1.9 eV collision energy are substantially different. The direct reaction occurs by the classical S_N2 reaction path, with Cl^- attacking the backside of CH_3I and directly displacing I^- (*8*). The indirect reaction occurs via a roundabout mechanism involving a CH_3 rotation. The principal mode for this mechanism is depicted in Fig. 3, where Cl^- first strikes the side of the CH_3 group, causing it to rotate around the more massive I atom. Then, after one CH_3 revolution, Cl^- attacks the C atom backside and directly displaces I^-. The time between the initial Cl^--CH_3 collision and the departure of I^- ranges around 400 fs. Two variants of the roundabout mechanism, of much lesser importance and with intermediate lifetimes of 1 to 4 ps, were also found. One is identical to the roundabout mechanism, except the departing I^- becomes transiently trapped in the post–reaction potential energy well (Fig. 1). The other is similar to the roundabout mechanism, except CH_3 rotates twice about the I atom. The translational energy partitioning for the roundabout mechanism approximates that of phase space theory (Fig. 2H), which assumes statistical dynamics. This suggests that this mechanism may participate in the statistical product energy partitioning observed for the $Cl^- + CH_3I$ S_N2 reaction at lower collision energies.

This combined experimental and computational study has identified a previously unknown roundabout, CH_3-rotation mechanism for gas-phase S_N2 nucleophilic substitution reactions. This mechanism may also play a role for other S_N2 reactions, such as the $Cl^- + CH_3Br$ reaction, where an energy-dependent change in the reaction mechanism has been discussed (*11*, *29*). It will be of particular interest to determine the role of the roundabout mechanism in other and more complex ion-molecule reactions.

References and Notes

1. See, for example, K. P. C. Vollhardt, N. E. Schore, *Organic Chemistry, Structure and Function* (Pallgrave Macmillan, Basingstoke, UK, 2007).
2. N. Merceron-Saffon, A. Baceiredo, H. Gornitzka, G. Bertrand, *Science* **301**, 1223 (2003).
3. B. Boudaïffa, P. Cloutier, D. Hunting, M. A. Huels, L. Sanche, *Science* **287**, 1658 (2000).
4. M. L. Chabinyc, S. L. Craig, C. K. Regan, J. I. Brauman, *Science* **279**, 1882 (1998).
5. J. K. Laerdahl, E. Uggerud, *Int. J. Mass Spectrom.* **214**, 277 (2002).
6. W. L. Hase, *Science* **266**, 998 (1994).
7. S. Schmatz, *ChemPhysChem* **5**, 600 (2004).
8. W. N. Olmstead, J. I. Brauman, *J. Am. Chem. Soc.* **99**, 4219 (1977).
9. C. H. DePuy, S. Gronert, A. Mullin, V. M. Bierbaum, *J. Am. Chem. Soc.* **112**, 8650 (1990).
10. J.-L. Le Garrec, B. R. Rowe, J. L. Queffelec, J. B. A. Mitchell, D. C. Clary, *J. Chem. Phys.* **107**, 1021 (1997).
11. L. A. Angel, K. M. Ervin, *J. Am. Chem. Soc.* **125**, 1014 (2003).
12. D. S. Tonner, T. B. McMahon, *J. Am. Chem. Soc.* **122**, 8783 (2000).
13. S. T. Graul, M. T. Bowers, *J. Am. Chem. Soc.* **116**, 3875 (1994).
14. A. A. Viggiano, R. A. Morris, J. S. Paschkewitz, J. F. Paulson, *J. Am. Chem. Soc.* **114**, 10477 (1992).
15. S. L. Craig, J. I. Brauman, *Science* **276**, 1536 (1997).
16. S. L. VanOrden, R. M. Pope, S. W. Buckner, *Org. Mass Spectrom.* **26**, 1003 (1991).
17. R. Wester, A. E. Bragg, A. V. Davis, D. M. Neumark, *J. Chem. Phys.* **119**, 10032 (2003).
18. L. Sun, K. Song, W. L. Hase, *Science* **296**, 875 (2002).
19. C. Hennig, S. Schmatz, *J. Chem. Phys.* **122**, 234307 (2005).
20. D. C. Clary, *Science* **279**, 1879 (1998).
21. P. Ayotte, J. Kim, J. A. Kelley, S. B. Nielsen, M. A. Johnson, *J. Am. Chem. Soc.* **121**, 6950 (1999).
22. J. Mikosch *et al.*, *Phys. Chem. Chem. Phys.* **8**, 2990 (2006).
23. J. J. Lin, J. Zhou, W. Shiu, K. Liu, *Science* **300**, 966 (2003).
24. Special care is taken to suppress formation of clusters in the supersonic expansion, as identified by photodissociation with ultraviolet (UV) laser light. Extraction fields are multistage to enable velocity mapping and spatial focusing of product ions spread over a large volume. The velocity distribution of the anion reactant beam is measured before and after recording each of the product velocity images. The velocity distribution of the neutral beam is measured by ionization with a pulsed electron beam and subsequent velocity map imaging. The beam spreads represent the largest contribution to the experimental resolution, such that effects of imperfect velocity mapping and slicing can be neglected. A few product anions are formed per bunch crossing; the repetition rate of the experiment is 10 Hz. We accounted for the decreased signal of fast product ions by using a one-dimensional, experimentally determined efficiency function.
25. W. J. Chesnavich, M. T. Bowers, *J. Chem. Phys.* **66**, 2306 (1977).
26. The aug-cc-pVDZ basis set was used for the C, H, and Cl atoms. For iodine, the Wadt and Hay effective core potential (ECP) was used for the core electrons and an uncontracted 3s,3p basis set for the valence electrons (*30*). This iodine basis was augmented by a d-polarization function with a 0.262 exponent and s, p, and d diffuse functions with exponents of 0.034, 0.039, and 0.0873, respectively (*31*). This basis is denoted as ECP/aug-cc-pVDZ in the text.
27. U. Lourderaj, K. Song, T. L. Windus, Y. Zhuang, W. L. Hase, *J. Chem. Phys.* **126**, 044105 (2007).
28. M. N. Glukhovtsev, A. Pross, L. Radom, *J. Am. Chem. Soc.* **118**, 6273 (1996).
29. Y. Wang, W. L. Hase, H. Wang, *J. Chem. Phys.* **118**, 2688 (2003).
30. W. R. Wadt, P. J. Hay, *J. Chem. Phys.* **82**, 284 (1985).
31. W.-P. Hu, D. G. Truhlar, *J. Phys. Chem.* **98**, 1049 (1994).

32. This work is supported by the Deutsche Forschungsgemeinschaft under contract no. WE 2661/4-1 and by the Eliteförderprogramm der Landesstiftung Baden-Württemberg. We thank U. Frühling and D. Schwalm for their support in setting up the experiment. The contribution from TTU is based on work supported by the NSF under grant no. CHE-0615321 and the Robert A. Welch Foundation under grant no. D-0005. Support was also provided by the TTU High-Performance Computing Center.

7 September 2007; accepted 12 November 2007
10.1126/science.1150238

Tidal Modulation of Nonvolcanic Tremor

Justin L. Rubinstein,[1]* Mario La Rocca,[2] John E. Vidale,[1] Kenneth C. Creager,[1] Aaron G. Wech[1]

Episodes of nonvolcanic tremor and accompanying slow slip recently have been observed in the subduction zones of Japan and Cascadia. In Cascadia, such episodes typically last a few weeks and differ from "normal" earthquakes in their source location and moment-duration scaling. The three most recent episodes in the Puget Sound/southern Vancouver Island portion of the Cascadia subduction zone were exceptionally well recorded. In each episode, we saw clear pulsing of tremor activity with periods of 12.4 and 24 to 25 hours, the same as the principal lunar and lunisolar tides. This indicates that the small stresses associated with the solid-earth and ocean tides influence the genesis of tremor much more effectively than they do the genesis of normal earthquakes. Because the lithostatic stresses are 10^5 times larger than those associated with the tides, we argue that tremor occurs on very weak faults.

Shortly after the discovery of both nonvolcanic tremor (*1*) and recurring slow-slip events (*2*, *3*), Rogers and Dragert determined that these two phenomena occur coincident with each other at regular intervals in the Cascadia subduction zone (*4*). They termed this phenomenon episodic tremor and slip (ETS). Soon thereafter, ETS was also observed in the Nankai Trough in Japan (*5*). ETS falls into a newly identified class of geophysical phenomena that are distinct from "normal" earthquakes. For these slow-slip phenomena, seismic moment scales with event duration (*6*), whereas for earthquakes, moment scales with the cube of event